Ann. For. Res. 66(1): 171-186, 2023
https://doi.org/10.15287/afr.2023.2700

ANNALS OF FOREST RESEARCH
www.afrjournal.org

Multi-temporal Pacific madrone leaf blight assessment with unoccupied aircraft systems

Matthew I. Barker[1], Jonathan D. Burnett[2], Tanya Haddad[3], William Hirsch[1], Dae Kun Kang[4], Kale'a Pawlak-Kjolhaug[5], Michael G. Wing[1]✉

Barker M.I., Burnett J.D., Haddad T., Hirsch W., Kun Kang D., Pawlak-Kjolhaug K., Wing M.G., 2023. Multi-temporal Pacific madrone leaf blight assessment with unoccupied aircraft systems. Ann. For. Res. 66(1): 171-186, 2023.

Abstract: Pacific madrone leaf blight (PMLB) is a contributing agent to the decline of Pacific madrone (*Arbutus menziesii*) trees. Multiple fungal pathogens cause PMLB, resulting in leaf spotting that can eventually kill leaves, increasing stress in individuals, and leaving them more susceptible to deadly cankers. Spores transmit via air and water droplets, particularly during wet Spring months. Unoccupied aircraft systems (UAS) technologies are in their relative infancy, but UAS are becoming more affordable and accessible. UAS promise increased efficiency in forest health monitoring applications, providing a safer aerial data collection method at a relatively-low cost when compared to occupied aircraft. In this study, we develop and present a UAS methodology to detect PMLB with a multispectral sensor. This methodology combines orthomosaic products derived from high-resolution (~4 cm) multirotor platform UAS multispectral imagery with machine learning and ground assessment of PMLB to classify visual presence of blight at the individual tree-level during multiple site revisits. The resulting model detected PMLB infection status of 29 field surveyed madrone trees with a kappa coefficient of , a balanced accuracy of 0.85, and a true positive rate of 0.92. The method presented here can be readily scaled to efficiently cover a much larger extent with a beyond-line-of-site capable UAS and minimal field sampling. The increased efficiency of this approach may be critical to characterizing PMLB in the near future as it is anticipated that PMLB prevalence will continue to increase as a result of climate change.

Keywords: *Phacidiopycnis washingtonensis, Arbutus menziesii,* Unoccupied aircraft systems, UAS, multispectral, leaf blight, disease detection, machine learning classifier.

Addresses: [1]Forest Engineering, Resources, and Management Department College of Forestry, Oregon State University, Corvallis, OR, USA. |[2]USDA Forest Service Pacific Northwest Research Station, Olympia, WA, USA. |[3]Computer Science, College of Engineering, Oregon State University, Corvallis, OR, USA. |[4]Civil & Construction Engineering, Geomatics Department, College of Engineering, Oregon State University, Corvallis, OR, USA. |[5]Geology Department, College of Earth, Ocean, and Atmospheric Sciences, Oregon State University, Corvallis, OR, USA.

✉**Corresponding Author:** Michael G. Wing (Michael.Wing@OregonState.edu).

Manuscript: received May 21, 2022; revised July 28, 2023; accepted July 31, 2023.

Introduction

Pacific Madrone Background

Pacific madrone (*Arbutus menziesii* Pursh) is a species of hardwood endemic to the Pacific northwest, USA and has been in a state of decline for the past decade due to the increased prevalence of multiple fungal pathogens, including *Phacidiopycnis washingtonensis* Xiao & Rogers, that cause Pacific madrone leaf blight (PMLB) (Elliott 1999, Sikdar et al. 2019). PMLB leaves the trees stressed and more susceptible to deadly canker diseases (*Fusicoccum* spp.) (Elliott et al. 2002). Under predicted climate change scenarios, it is expected some madrone populations will be lost as a result of changing temperatures and precipitation associated with climate change (Elliott et al. 2012). The species is characterized by the burnt-orange hue of its bark which peels away on younger growth to uncover a light green color. The range of Pacific madrone extends from southern California to Vancouver, B.C., and can be found west of the Cascade Range in Oregon, U.S.A. Madrone retains its leaves throughout the year, sprouting new growth in the spring. Madrone produces bright red berries and light-colored flowers which grow at the ends of its branches. Its sprouts provide some value to browsers including sheep, goats, and deer while its berries are a food source for deer and many bird species (Sampson & Jesperson 1963). Additionally, it provides habitat for cavity nesters including woodpeckers and wrens (Reeves 2007). Madrone is commercially valued for use in veneers, flooring, and other non-structural uses (USDA 2006), and is employed for erosion control and valued for its aesthetic beauty in landscaping, growing in sites with well-drained, rocky soils that experience little shade (Bennett & Shaw 2008).

Foliar Blight

Blight has been implicated as one of the leading factors in the widespread decline of Pacific madrone (Elliott et al. 2012). The plant's foliage is host to a variety of fungal pathogens that colonize young leaves, spreading via spores in air or water primarily during spring rains (Bennett & Shaw 2008). Fungi that infect Pacific madrones manifest in the form of discoloration, spots, and galls on foliage. Disease can increase a tree's susceptibility to further colonization by fungi. It has been shown that infection of *A. menziesii* by the pathogenic oomycete *Phytophthora ramorum* followed by secondary infection by *Botryosphaeria dothidea* resulted in greater mortality than infection by either species alone (Maloney et al. 2004).

Pacific madrone is known to be sensitive to foliage diseases caused by fungal organisms, which can be transmitted via airborne or water-splashed spores during wet weather (Bennett & Shaw 2008). Such diseases often cause leaf spots that can grow into foliage blight, killing entire leaves. Root diseases can also affect foliage loss or curl and are associated with moist soil conditions found in overwatered, heavy clay, or poorly drained soils. Deep infrequent watering is considered preferable to frequent light watering for overall madrone health. Although madrones are relatively drought tolerant, extended periods of drought can increase disease susceptibility in trees.

Detection and management of PMLB by raking and destroying impacted foliage is an approach that can fortify madrone populations as blight-impacted individuals are more susceptible to more severe disease and stress associated with climate change (Bennett & Shaw 2008, Elliott et al. 2012). Conventional PMLB survey methods are field-centric which are costly due to the need to survey trees individually and time and expense associated with accessing remote sites upon which they grow. Individual tree assessment is necessary because detection of PMLB can dictate which trees managers should focus control measures like leaf raking and burning efforts to mitigate the spread of the disease

(Bennett & Shaw 2008). Additionally, human activity represents a potential vector for further spreading disease when they move through an infected site (Lucas & Dickinson 1998). With the growing popularity and accessibility of unoccupied aircraft systems (UAS) for remotely sensing environmental phenomena, there exists an unexplored opportunity for increasing PMLB survey efficiency by remotely conducting individual tree assessments while simultaneously reducing the risk of exacerbating PMLB spread through anthropogenic vectors.

Pertinent Previous Findings

UAS are popular in environmental monitoring applications because they are inexpensive compared to occupied aircraft and capable of rapidly surveying large areas in a short time. UAS remote sensing has been shown to enable efficient acquisition of forest inventory data at lower costs and with more detail than ground-based inventories (Guimarães et al. 2020). Common products from such surveys characterize physical attributes of trees via elevation models, ortho-imagery, and point clouds, with calculation of vegetation indices and use of spectral signatures also common. In forest health monitoring for disease detection, the most common platforms are vertical takeoff and landing (VTOL) vehicles with true-color (i.e., red, green, blue wavelength (RGB)) sensors.

Repeat UAS remote sensing surveys have succeeded in facilitating multi-temporal change detection. Marques et al. (2019) employed a method to extract features from UAS-derived color-infrared (CIR) and true-color orthoimagery with a resolution of 16 cm ground sampling distance (GSD) to conduct a multitemporal analysis of chestnut trees. Results showed 98% success in detecting individual chestnut trees. Additionally, the strong relationship between ground observations and UAS-derived tree height and diameter evidenced by R^2 correlation coefficients of 0.79 and 0.92, respectively, were indicative that UAS estimates of biophysical attributes would be sufficient for examining change at tree-level through time.

Extracting physiologically relevant vegetation indices (VIs) from remotely sensed data has been effectively utilized in disease detection. For example, Marin et al. (2018) found vegetation indices derived from the Landsat 8 Operational Land Imager and Thermal Infrared Sensor to be highly correlated with disease incidence of bacterial blight of coffee ($r = 0.76$) and disease severity ($r = 0.52$). When paired with high resolution data originating from UAS, VIs have been effectively employed to classify disease severity of *Verticillium* wilt at various stages in olive trees (Calderón et al. 2013). Zarco-Tejada et al. (2012) investigated water stress detection in a citrus orchard and demonstrated the feasibility of thermal, narrow-band indices, and micro-hyperspectral imaging via small UAS for stress detection in a heterogeneous tree canopy where very high resolution is required. Di Nisio et al. (2020) investigated 71 olive trees impacted with olive quick decline syndrome using multispectral, thermal, and high-resolution visible sensors. They calculated RGB, CIR, and NDVI indices from UAS imagery, and a Sørensen-Dice similarity coefficient for each olive tree after tree segmentation. High Sørsensen-Dice coefficients indicated successful tree delineation noting NDVI alone was not sufficient for segmentation and olive quick decline syndrome classifier performed well with 98% sensitivity and 100% specificity. Additionally, Garza et al. (2020) found the correlation between UAS-derived triangular greenness index (TGI) and field health measurements of citrus trees useful to assess tree health and disease status.

UAS technology has additionally been used in previous studies to detect blight in a variety of species. Bagheri (2020) investigated a UAS equipped with a multispectral sensor to identify fire blight in 75 pear trees at different levels of

disease achieving classification accuracies for healthy, asymptomatic, and symptomatic trees of 98.7%, 91.4%, and 93.9%, respectively. Sandino et al. (2018) combined UAS aerial mapping, a hyperspectral sensor, and machine learning to detect and classify myrtle rust (*Austropuccinia psidii*) in paperbark trees (*Melaleuca quinquenervia*), achieving detection rates of 97.24% for healthy trees and 94.72% for affected trees.

Our objectives are to demonstrate the utility of combining machine learning methods with UAS multi-spectral remote sensing data for individual tree surveys of PMLB. We quantified the relationship between field observed blight impact on 29 trees and remotely sensed spectral signatures of individual madrone crowns across a common garden site for three years using a machine learning model development method. We then used the resulting model to assess PMLB disease status of all 1,349 trees in the site for the purpose of evaluating spatio-temporal trends in PMLB. We are unaware of any previous peer-reviewed literature that has applied UAS remote sensing data and machine learning for PMLB assessment.

Materials and Methods

Site and Data Acquisition

The Pacific madrone study area is one site in a common garden study intended to gather data regarding various genetic traits of 105 Pacific madrone families from 7 ecoregions using seed Washington State University collected from 2006 to 2010. Researchers sowed plug trays in February 2011 and moved them to a greenhouse in April 2011. In June 2011, they germinated seeds grown in containers and placed them outside until they transplanted them in fall and winter 2011. Genetic traits examined included but were not limited to disease resistance, growth traits, and suitability to predicted conditions under climate change scenarios (Elliott et al. 2012). The site is located on privately owned land located north of Corvallis, Oregon, USA near N 44°43', W 123°23' (Figure 1). The study site is approximately 1.5 ha (3.6 acres) in area with a modest elevation gradient ranging between 235 and 247 m. According to precipitation data acquired from PRISM Climate Group (2022), annual precipitation in the area was 1187 mm, 1411 mm, and 1585 mm for 2019, 2020, and 2021, respectively. We conducted field and aerial surveys during five site visits occurring on October 15, 2019, May 28, 2020, October 15, 2020, May 28, 2021, and October 15, 2021, between approximately 12:00 and 15:00 PDT. The October 2019 flights occurred during scattered cloud conditions, and the May 2020, October 2020, May 2021, and October 2021 flights during clear skies.

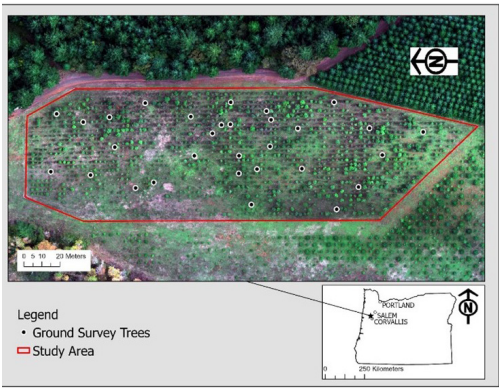

Figure 1 Study Site – Pacific madrone plantation in northwest Oregon, USA. Points are locations of 29 field validation trees. Background is orthomosaic from UAS imagery flown in Oct. 2019.

Ground Survey

We selected and surveyed 30 trees for field validation, hereafter referred to as ground survey trees. The ground surveys facilitated model training and validation described later. We revisited the same ground survey trees during each site visit. We selected ground survey trees that encompassed a broad spatial distribution and displayed the full range of visible signs of infection, ranging from few visible signs to clearly affected. We stem mapped and georeferenced ground survey trees with a Trimble Geo XH global navigation satellite system receiver paired with a range

pole-mounted external Tornado antenna. We assessed blight and measured height of each ground survey tree during each visit. We measured tree height with a measurement pole from base of stem to the highest point of each tree. We followed the blight assessment from DeWald et al. (2018) and is as follows: (1) Identify the most severely impacted leaf from current season growth and classify **severity** according to percentage of leaf area (0%, <25%, 25%-50%, >50%) exhibiting signs of blight. (2) Estimate incidence by visually examining the entire crown and estimating the percentage of tree leaves affected (<25, 25-50, 51-75, >75) by the most severe rating identified in step 1 (DeWald et al. 2018). (3) The incidence data is then used to assign a dominant severity class to each surveyed tree, and when two equally dominant severity classes are apparent, the most severe class is reported. We then tallied severity classes by survey date to characterize PMLB severity (Table 1).

Due to all surveyed trees having a visual severity rating greater than 50%, we modified DeWald et al.'s approach to increase levels of gradation to better correspond with the continuous response of the indicator variables in the remotely sensed data. We incorporated current year incidence to provide a distinction between blight impacts from previous years. This accounts for the disproportionately large influence the leaves from the most recent growing year has on the remotely sensed signal relative the proportion to total leaf area, owing to the fact that most recent growing year's leaves represent the largest proportion of the visible crown when viewed from above at nadir.

Given the relatively few observations in the intermediate severity classes of <25 and 25-50, we consolidated severity classes into two blight classes based on incidence, No Visual Blight (NVB) and Visual Blight (VB). We assigned blight class NVB to ground surveyed trees with blight severity class of 'Blight 0' and incidence > 50, i.e., greater than 50% of the current year's foliage presented leaves of blight severity 0. The Blight Class VB was assigned to all remaining observations, i.e., greater than 50% of the current growth presented visually symptomatic leaves (Table 2). One ground surveyed tree fell as a result of wind damage during 2021, thereby reducing our ground surveyed trees from 30 to 29. This resulted in a total of 145 field observations, each labeled with blight class and corresponding date of the

Table 1 PMLB Severity: Four Class Distribution Table.

Date	Severity	Count	Date	Severity	Count	Date	Severity	Count
10/15/2019	Blight 0	13	5/28/2020	Blight 0	10	5/28/2021	Blight 0	27
10/15/2019	Blight >0-<25	5	5/28/2020	Blight >0-<25	0	5/28/2021	Blight >0-<25	0
10/15/2019	Blight 25-<50	2	5/28/2020	Blight 25-<50	0	5/28/2021	Blight 25-<50	0
10/15/2019	Blight 50	9	5/28/2020	Blight 50	19	5/28/2021	Blight 50	2
			10/15/2020	Blight 0	15	10/15/2021	Blight 0	26
			10/15/2020	Blight >0-<25	2	10/15/2021	Blight >0-<25	2
			10/15/2020	Blight 25-<50	0	10/15/2021	Blight 25-<50	1
			10/15/2020	Blight 50	12	10/15/2021	Blight 50	0

Table 2 PMLB Severity: Two Class Distribution Table.

Date	Blight Class	Count	Date	Blight Class	Count	Date	Blight Class	Count
10/15/2019	NVB	3	5/28/2020	NVB	4	5/28/2021	NVB	25
10/15/2019	VB	26	5/28/2020	VB	25	5/28/2021	VB	4
			10/15/2020	NVB	3	10/15/2021	NVB	24
			10/15/2020	VB	26	10/15/2021	VB	5

observation for each of the 29 trees measured and remeasured over the five observation events (Table 2). Table 2 is derived from observations associated with the complete severity and incidence table of 29 survey trees provided in supporting information.

Aerial Survey

We collected remotely sensed imagery using a Micasense Altum multispectral camera (Micasense 2020) onboard a DJI Matrice 200 v2 quadcopter UAS (DJI 2019). The Altum is a six-band camera sensitive to red, green, blue, near infrared, red-edge, and longwave infrared (i.e., thermal). Imaging resolution is 4.3 cm and 67.8 cm ground sampling distance at 100 m above ground level (AGL) for the first five bands and thermal band, respectively. Detailed Matrice and Altum flight and imaging specifications are described by Wing (2019).

We conducted UAS flights autonomously with DJI Pilot software (DJI 2020) to ensure necessary image forward overlap and side overlap were achieved. Flights were approximately 8 minutes in duration to cover the entire study site. This software allows for user-provided specifications on flight area, velocity, image overlap, and altitude. Flight altitude was set to 100 m AGL, ground velocity was set at 5 m/s, and forward and side overlap were both specified at 80%. This level of forward and side overlap results in approximately 25 overlapping images of any given location in the study area which produces the most geometrically accurate orthomosaics (Hostens et al. 2022; Nesbit & Hugenholtz 2019). We imaged a spectral calibration target with the multispectral sensor immediately before and after each flight to calibrate the five non-thermal bands and convert imagery data to time-invariant at-sensor reflectance which facilitated comparison of images taken on different dates.

Image Processing

Image processing was accomplished with Agisoft Metashape (2019) photogrammetry software with processing parameters based on the sensor manufacturer's recommendations (Micasense 2019, July 25). We applied a radiometric calibration to imagery during Metashape processing by sourcing the spectral calibration target images taken during each flight and specifying manufacture-provided albedo values. We converted the five non-thermal bands from 16 bit digital numbers to surface reflectance values between 0.0 and 1.0, where 1 is equivalent to 100% reflectance of incident light for the specified band and converted thermal values from centi-Kelvin to Celsius (cK/100 – 273.15) for more intuitive interpretation. The resulting six-band orthomosaic image raster files had resolutions of approximately 5 cm GSD. Note that the thermal band is automatically resampled from 67.8 cm GSD to match GSD of the non-thermal bands using the nearest neighbor assignment method.

The resulting orthomosaics were imported to R (R Core Team 2021) using the Raster package (Hijmans 2021) to conduct a series of calculations necessary to produce nine VIs that are known to indicate structural and/or physiological condition of vegetation (Table 3). This expanded the original six bands to a total of 15.

Tree Crown Delineation and VI Extraction with GIS Software

We utilized ArcGIS Pro version 2.8.3 (Esri 2021) to manually delineate 1,349 tree crowns by generating circular buffers, where circle radius and center were manually measured and identified for each tree using the true color orthomosaic from October 2019 as a reference. The 29 ground survey trees were associated with a corresponding tree crown in ArcGIS using the GPS position to provide labeled training data for the supervised classification model described in the next section. We exported tree crown circles into the R environment and used the exactextractr

Table 3 Vegetation indices constructed from individual bands 1-6. Formula describes how vegetation. indices are derived and reference denotes the source of the VI.

Band	Name or Vegetation Index	Formula*	Reference
1	Blue (R_b)	From sensor	NA
2	Green (R_g)	From sensor	NA
3	Red (R_r)	From sensor	NA
4	Red edge (R_{re})	From sensor	NA
5	Near infrared (R_{nir})	From sensor	NA
6	Longwave infrared (LWIR)	From sensor	NA
7	Triangular Greenness Index (TGI)	$TGI = -0.5[(\lambda r-\lambda b)(Rr-Rg)-(\lambda r-\lambda g)(Rr-Rb)]$	(Hunt et al. 2011), Hunt et al. (2013)
8	Green Red Vegetation Index (GRVI)	$GRVI = \frac{R_g - R_r}{R_g + R_r}$	Tucker (1979)
9	Normalized Difference Vegetation Index (NDVI)	$NDVI = \frac{R_{nir} - R_r}{R_{nir} + R_r}$	Rouse et al. (1974)
10	Normalized Difference Red Edge (NDRE)	$NDRE = \frac{R_{nir} - R_{re}}{R_{nir} + R_{re}}$	Barnes et al. (2000)
11	Green Normalized Difference Vegetation Index (GNDVI)	$GNDVI = \frac{R_{nir} - R_g}{R_{nir} + R_g}$	Gitelson et al. (1996)
12	Modified Simple Ratio Index (MSR)	$MSR = \frac{\frac{R_{nir}}{R_r} - 1}{\sqrt{\left(\frac{R_{nir}}{R_r} + 1\right)}}$	Chen (1996)
13	Modified Simple Ratio Index Red Edge (MSRE)	$MSRE = \frac{\frac{R_{nir}}{R_{re}} - 1}{\sqrt{\left(\frac{R_{nir}}{R_{re}} + 1\right)}}$	Cao et al. (2013)
14	Green Chlorophyll Index (GCI)	$GCI = \frac{R_{nir}}{R_g} - 1$	Gitelson et al. (2005)
15	Red Edge Chlorophyll Index (RECI)	$RECI = \frac{R_{nir}}{R_{re}} - 1$	Gitelson et al. (2005)

Note: * λ is wavelength associated with band and R is reflectance of corresponding band: blue (b), green (g), red I, red edge (re), near infrared (nir).

tool (Baston 2021) to calculate mean of each of the 15 bands (Table 3) for each of the given time periods. Each tree circle received a mean for each raster band and date (i.e., factors indicating month and year).

Model

The aim of this study was to develop a Pacific madrone leaf blight detection model based on remote sensing that would facilitate understanding of the site-wide condition of the madrone stand using the full population of trees rather than the limited number of ground survey trees. To this end we utilized the Ranger (Wright & Ziegler 2017) implementation of the Random Forest (Breiman 2001) supervised classification model development algorithm. All modeling was conducted in the R environment (R Core Team 2021), and we used the Caret package (Kuhn 2019) because it facilitates extraction of numerous model performance metrics, hyperparameter tuning, and supports a number of different cross-validation routines. We selected the Random Forest (RF) algorithm to classify blight because it is increasingly popular in environmental remote sensing fields due to it being robust to assumption violations that tend to hamstring conventional linear models such as multi-collinearity, non-linearity, and unspecified interactions. Random Forest works by building an ensemble of many weak

decision tree learners and using the calculated proportion of correct and incorrect learners to inform splits in the covariate data that explain the relationship between model covariates and observed response. Additionally, RF produces unbiased out-of-bag (OOB) estimates of model performance based on held-out independent observation data (Zhang et al. 2010). We used the Ranger implementation because it is natively supported in the Caret package (Kuhn 2019) we used for constructing the model, and in testing Ranger is faster than other RF implementations, due in part to its use of multi-threading and parallelization.

We fit a single binomial classification RF model to the 29 ground survey trees, incorporating means from 15 remotely sensed bands, time variables for month and year, and spatial x, y coordinates (Equation 1). Rather than create five separate models, we incorporated month and year into the model to maximize the range of madrone crown condition captured by the remotely sensed data. Additionally, we evaluated model performance with 100 repeats of a 5-fold cross-validation (CV) routine rather than simple data splitting to make use of the limited amount of observation data because it has been shown to be unbiased (Kuhn 2019). We chose to use 100 repeats in order to produce a distribution of means from the 5-fold CV runs, resulting in estimates that are more stable than a single 5-fold CV routine and thus robust to the influence associated with randomly reshuffling the data. 5-fold is a common implementation of the k-fold method and represents an optimization of computational efficiency that facilitates testing against 20% of the data on each fold.

Nested within each CV routine was a hyperparameter tuning grid that evaluated the optimal value of mtry between 2 and 15, and the optimal minimum node size between three and five. MTRY is important to optimize, especially in high dimensionality data because it can affect importance values of highly correlated predictors, introducing bias when assessing variable importance (Strobl et al. 2007). Minimum node size is important in a prediction or detection model because it further minimizes potential for Random Forest to overfit the model to a single extreme observation. We did not tune number of trees, opting to hold this value constant at 500 trees. The split rule was set to extratrees, an implementation of extremely randomized trees by Geurts et al. (2006). This implementation of RF randomly selects the point at which to split features from a subset of data, averaging the value to increase accuracy and reduce overfitting, whereas random forest traditionally optimized this value based on Gini for each resample of the data.

Following the model training, we calculated normalized variable importance to assess the relative importance of predictor variables on the resulting classifier. We also calculated prediction accuracy for out-of-bag data, permuting each predictor variable. The statistical software calculated differences in accuracies for each random forest tree, then averaged these values. We plotted variable importance to visualize the relative importance of each covariate to the model.

We used the partial function in the pdp package by Greenwell (2017) to calculate partial dependence for each spectral variable. Partial dependence plots allow for the visualization of the relative impact of a subset of independent

Equation 1:

$$\textbf{\textit{Blight Class}} \sim R_b + R_g + R_r + R_{re} + R_{nir} + LWIR + TGI + GRVI + NDVI + NDRE + GNDVI + MSR + MSRE + GCI + RECI + \textbf{\textit{Time}}_{Month} + \textbf{\textit{Time}}_{Year} + Coordinate_x + Coordinate_y$$

Variables in bold are factors. Blight Class has 2 levels: NVB and VB, month has two levels: October and May, Year has three levels: 2019, 2020, and 2021.

variables with regard to the dependent variable (Friedman 2001). These plots can provide insight regarding the influence of independent variables to prediction outcomes but do not provide the degree of interpretation gleaned from coefficients of parametric models (e.g., linear regression).

Analyses

We evaluated the classification performance of the model using Cohen's kappa (Cohen 1960), balanced accuracy (Brodersen et al. 2010), and the confusion matrix (Ting 2017). We assessed prediction error using the out-of-bag (OOB) estimates produced from Random Forest. Additionally, we created and assessed a variable importance plot to understand which predictor variables are most important to blight detection. Lastly, partial dependence plots for the top three variables demonstrate how change in these variables drive the likelihood of blight.

We used the RF model to predict blight class (i.e., NVB, VB) for the 1,320 trees not having field observations, for each of the five month and year combinations. Data were subsequently summarized to infer stand-level blight status by estimating the percentage of NVB and VB from the individual tree blight class assessments generated from the predictions.

Results

Random Forest

RF classification performance of the model based on the confusion matrix from the 100 repeat 5-fold CV (Table 4) is as follows: kappa = 0.71 (95% CI 0.70, 0.72), balanced accuracy 0.85, and OOB prediction error = 0.11. The true positive rate was VB 0.92, which is higher than the true NVB rate of 0.78. Tuned final model parameters are as follows: mtry = 3 and minimum node size = 5.

Table 4 Confusion Matrix: Aggregated cell counts and percentual average cell counts across resamples on 100 repeats of 5-fold CV. Cells on the diagonal axis indicate ground survey trees correctly classified by the RF model.

		Reference	
		NVB	VB
Prediction	NVB	4652 (32.1%)	768 (5.3%)
	VB	1248 (8.6%)	7832 (54.0%)
Balanced accuracy = 0.85			

Variable Importance and Partial Dependence

Predictors with the highest influence were indicator variables for year, followed by mean at-sensor reflectance in the red and blue bands, an indicator variable for month, and mean radiant temperature from the LWIR band (Figure 2). Partial dependence plots of spectral predictors are presented below and organized in descending order of importance from left to right, top to bottom to correspond with variable importance rankings (Figure 3).

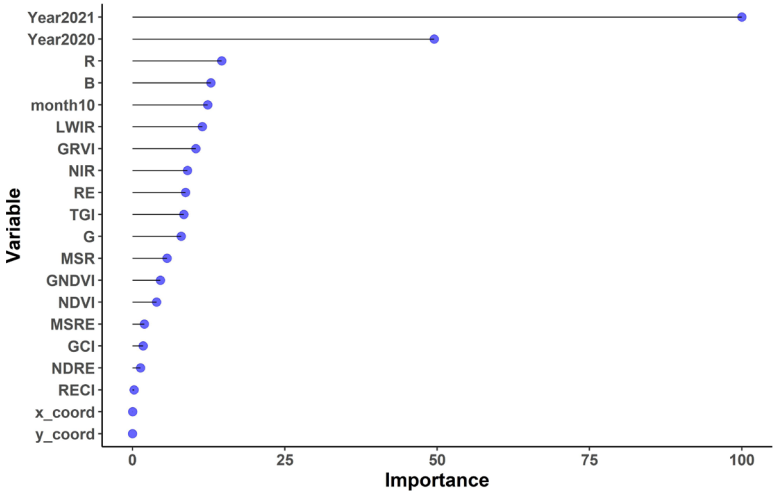

Figure 2 Variable Importance Plot, values are normalized by standard error.

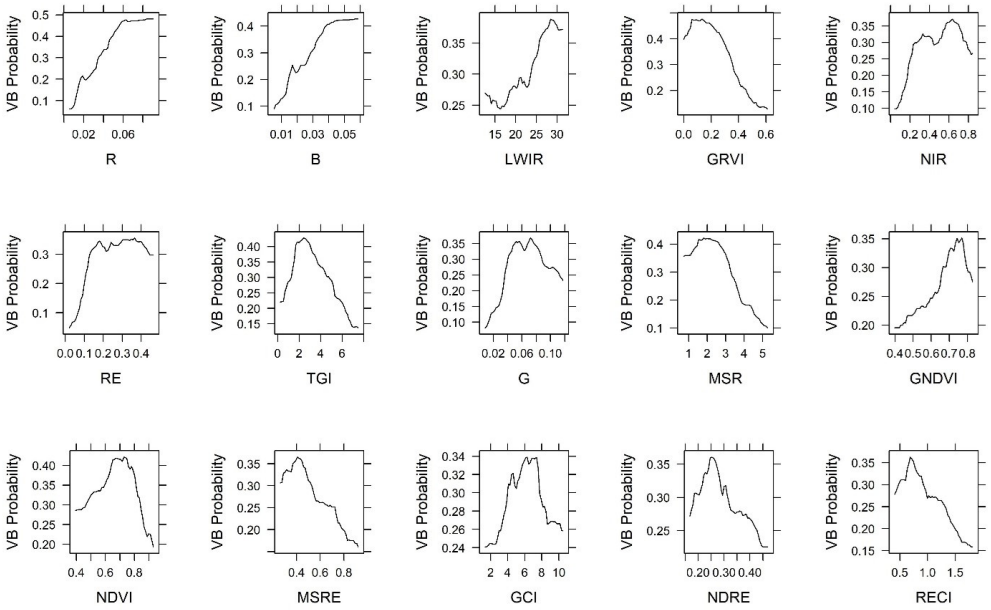

Figure 3 Partial Dependence Plots for Spectral Predictors.

Model Predictions

We used the final RF model to predict blight class for all 1,349 trees recorded during each UAS flight. We visualized the associated percentages of blight class we observed in the field and the percentages from the random forest predicted results as a stacked bar chart (Figure 4).

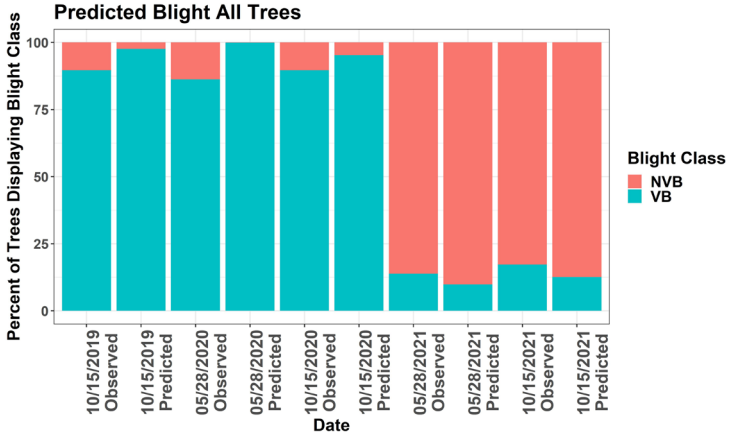

Figure 4 Percentual Distributions of Predicted (1,349 trees) and Observed (29 Ground Survey Trees) Blight Class. Y-axis is the combined percentage of trees displaying no-visible blight (NVB) or visible blight (VB) with NVB in red and VB in green. In 2021 NVB trees dominate the stand which may indicate that most of the blighted leaves have abscised leaving only the healthy green current-year foliage.

Discussion

Model Performance

The final random forest model demonstrated a substantial level of agreement at kappa = 0.71 between the predicted results of the classifier and the reference data based on the Kappa scale in (Landis & Koch 1977). Cohen's kappa is considered an adequate measure of model performance and assesses the level of agreement between predicted classes of the trained model and observed classes for a subset of testing data because it accounts for the likelihood of achieving agreement from random chance. A kappa of 0 would indicate the model performed no better than we would

anticipate due to random chance, whereas 1 indicates a perfect classifier. The substantial level of agreement between field observations and model predictions as evidenced by the balanced accuracy metric suggests the model is performing suitably well to make predictions to all madrone trees in one site.

Of the trees the model identified as impacted by blight, 21% of these trees did not visually present as impacted by the disease. Conversely, 9% of the trees identified by the model to be clear of blight were impacted. The false negative warrants higher concern because failing to detect a PMLB-positive individual would result in a missed opportunity to rake and burn the impacted foliage associated with the impacted tree, resulting in further spread of blight to neighboring trees. False positives are less of a concern because a trained crew would ignore the tree and move to the next blight-impacted tree.

Relative Importance of Predictors

When we examined the relative importance of the various predictors regarding their individual effects on model accuracy, indicator variables for year and month comprised three of the five most important predictors. Temporal variables encapsulated intra-temporal variation within the site. This may include aspects of weather like precipitation and temperature that affect the spread of blight throughout among trees throughout the site. Additionally, there may be a lag effect associated with the two years of drought the site experienced culminating in a decrease in visible blight as the pathogen had diminished opportunity to spread via water particles.

Spectral predictors including mean reflectance in red and blue bands had relatively high importance to model accuracy. Intuitively, chlorophyll associated with healthy foliage absorbs blue and red energy of the electromagnetic spectrum (centered at 0.45 μm and 0.67 μm respectively), reflecting green energy, thereby resulting in a visibly green appearance to the human eye. Whereas a leaf associated with a stressed plant exhibits a red appearance as it undergoes less chlorophyl production, decreasing absorption in red and blue (Lillesand et al. 2015). The variable importance plot suggests the model is discerning the nuanced spectral pattern of leaves impacted by blight through mean reflectance in these individual bands. Interestingly, mean radiant temperature recorded in the LWIR band is also an important variable. Reduced transpiration rates of diseased leaves can be detected in the LWIR region of the electromagnetic spectrum (Oerke et al. 2010).

Mean reflectance in red and blue bands and radiant temperature recorded in the LWIR band are the spectral variables exhibiting a broad range that correlate with the response (Figure 3). Potential pixel mixing may explain the difficulties the model is experiencing where we notice a parabolic trend in the spectral data (e.g., TGI). Variable importance shows relative less importance associated with the noisy variables that have very weak relationships to the observed response. The range of mean reflectance values in the partial dependence plots (Figure 3) are consistent with spectral reflectance curves of other hardwoods (Kalensky & Wilson 1975, Lillesand et al. 2015). This range of values suggests the reflectance calibration is performing well enough that confounding influence from potential variation in bi-directional reflectance from the five different aerial surveys is not significant enough to impact the results of the multi-temporal analysis.

Predicted and Observed Blight Distribution

Applying the RF classifier to the 1,349 trees on the site produced distributions of VB and NVB like those in the ground survey data (Figure 4). Both revisits in 2021 suggest a significant decline in PMLB prevalence throughout the site compared to visits that occurred in 2019 and 2020, possibly owing to the reduced drought conditions compared to the previous

two years. 2021 experienced the greatest annual precipitation at 1585 mm compared to the other two years, with 2020 falling just short at 1411 mm, while 2019 lagged significantly at 1187 mm. When we examine how mean precipitation for these years compare to PRISM Climate Group's (2022) 30-year normal (calculated from mean annual precipitation from 1991-2020) of 1542 mm, both 2019 and 2020 were relative drought years experiencing 75% and 89% annual precipitation compared to 30-year normal. Whereas 2021 was a slightly wetter than average year at 103%. Although blight is thought to spread via water droplets, it warrants further investigation to determine whether drought-stressed madrones are more susceptible to pathogens that cause the disease especially as hydrological drought frequency is projected to increase over the course of the 21st century (Strzepek et al. 2010).

Any individual year's results may be useful for informing management decisions. Managers may opt to remove impacted foliage by either removing entire trees or raking and burning impacted foliage near the blighted individuals in areas where a high density of probable blight impacted trees are identified (i.e., VB). It is worth noting that in 2021 the site appeared to recover suggesting that managers may want to consider a longer-term trend (e.g., 3 to 5 years) of blight status before deciding to implement any destructive or costly intervention measures. However, it could be that the reduction of VB in 2021 is not a recovery at all but the result of the abscission of all visibly infected trees leaving the current year's growth which is visually asymptomatic at the time of survey. Additional study examining changes in leaf area, leafy biomass, and age of distribution of retained leaves would be necessary would be necessary to draw more concrete conclusions.

Given the increased accessibility of UAS technology (Wing et al. 2013), the relatively inexpensive access to computational power (PC meeting the minimum requirements for running Agisoft Metashape costs less than $1500 at the time of this writing), and free and open-source nature of Random Forest modeling via the R environment, we assert that the methods presented here can be reasonably applied by resource managers who have qualified personnel available. For those who do not possess in-house UAS capabilities there are numerous UAS survey firms available within the continental United States and elsewhere. For those who lack the statistical modeling expertise, we have provided the workflow for reproducing the model and provide the code for fitting the model and conducting predictions. Additionally, the method requires someone with expertise using GIS for summarizing and producing mapping outputs in an operational manner.

Efficacy of PMLB Detection for Information Management Decisions

The UAS methodology presented here is intended to be incorporated with a limited field survey, not replace it entirely. We expect the presented method would not adequately detect PMLB without providing temporally synchronized field training data to constrain the model. With the addition of more temporal data in the form of follow-up flights and surveys the model would need to be refitted with the new data to account for potential variability captured during that date. This is a limitation of the method because predictions are confined to the months and years for which we have observation data. If replicated over an expanded area, it is likely that more than 30 ground observations would be necessary to facilitate the development of a model that adequately detects PMLB. Practitioners intending to replicate this method should be aware that a substantial portion of the time saved in the field is simply transferred to time in front of the computer. However, computer time is inherently safer than field time and does not incur a multi-hour transportation cost. Furthermore, once the method is fully developed, the computer time would be reduced through continued refinement and

analyst experience. The ground survey of 29 trees typically took a team of four two hours to complete while flights required fewer than 30 minutes including setup and takedown. Additionally, image processing, crown delineation, and model development require less than 10 hours after establishing a workflow from this case study. Based on the results of our work, it is reasonable to expect that a UAS survey and associated ground survey would be able to cover more trees and facilitate inference about PMLB status over a larger area than a ground survey alone. Area coverage can be substantially increased by incorporating a vertical takeoff and landing fixed-wing platform. Manufacturers like Wingtra advertise coverage of anywhere from 500-600 acres in a single 1-hour flight at the legal altitude ceiling of 120 m depending on sensor (Wingtra 2022). Pairing emerging UAS platforms such as this with multispectral sensors and machine learning models like those presented here may augment detection surveys of foliar diseases such as PMLB, providing robust monitoring solutions to detect and manage these problems.

Conclusions

We presented a methodology for supplementing field assessments of PMLB with spectral and thermal data recorded with a UAS-mounted multispectral sensor. This process produces a classifier capable of extending data associated with the ground survey trees to facilitate making inference about the blight status of all trees on site. Additionally, we were able to account for intra-flight variability by including variation as a temporal component in the form of year and month in the random forest classifier. By incorporating UAS into a PMLB detection workflow, managers can determine probable blight status at the tree-level, thereby informing mitigation efforts to control the spread of the pathogens. We anticipate this approach could be utilized to detect pathogens in other plant species that visually present as foliar spotting. This approach does not detect blight prior to presentation of visual symptoms, but future studies may build on this work by incorporating PCR tests of foliage for trees that are not displaying visual symptoms and investigating whether sensors and machine learning algorithms are able to detect blight positive individuals prior to visual symptoms. Future research may further improve on our methodology by incorporating a quantitative field component to assess blight impact such as a field spectrometer rather than the subjective blight assessment we conducted. The RF model used to predict trees displaying visible blight symptoms does not provide the insight one may glean from parametric models, e.g., linear regression. Consequently, we are unable to estimate the correlations between spectral values and blight. However, variable importance and partial dependence plots do provide some insight into the value of those variables as they pertain to the final model used to generate predictions. The results of this case study culminate in a tool to predict visible blight class from UAS imagery that may be incorporated into a blight assessment, thereby expediting the detection process.

Acknowledgements

The authors wish to thank Starker Forests for permitting us access to the Pacific madrone stand. Additionally, the first author expresses sincere gratitude to Bryan Begay, Katie Nicolato, Sudeera Wickramarathna, and Michael Winfield for their continued assistance in repeat field surveys. We also wish to thank Richard Sniezko for sharing the foliar blight assessment.

Declaration of the authors

The authors declare there is no conflict of interest regarding the publishing of the paper, which does not include any form of plagiarism.

References

Agisoft 2019. Agisoft Metashape. Available from https://www.agisoft.com/

Bagheri N. 2020. Application of aerial remote sensing

technology for detection of fire blight infected pear trees. Computers and Electronics in Agriculture 168: 105147. https://doi.org/10.1016/j.compag.2019.105147.

Barnes E., Clarke T.R., Richards S.E., Colaizzi P., Haberland J., Kostrzewski M., Waller P., Choi C., Riley E., and Thompson T.L. 2000. Coincident detection of crop water stress, nitrogen status, and canopy density using ground based multispectral data.

Baston D. 2021. exactextractr: Fast Extraction from Raster Datasets using Polygons.

Bennett M. and Shaw D.C. 2008. Diseases and insect pests of Pacific madrone. [Corvallis, Or.]: Oregon State University, Extension Service.

Breiman L. 2001. Random Forests. Machine Learning 45(1): 5-32. https://doi.org/10.1023/A:1010933404324.

Brodersen K.H., Ong C.S., Stephan K.E., and Buhmann J.M. 2010. The Balanced Accuracy and Its Posterior Distribution. *In* 2010 20th International Conference on Pattern Recognition. 23-26 Aug. 2010, pp. 3121-3124.

Calderón R., Navas-Cortés J.A., Lucena C., and Zarco-Tejada P.J. 2013. High-resolution airborne hyperspectral and thermal imagery for early detection of Verticillium wilt of olive using fluorescence, temperature and narrow-band spectral indices. Remote Sensing of Environment 139: 231-245. https://doi.org/10.1016/j.rse.2013.07.031.

Cao Q., Miao Y., Wang H., Huang S., Cheng S., Khosla R., and Jiang R. 2013. Non-destructive estimation of rice plant nitrogen status with Crop Circle multispectral active canopy sensor. Field Crops Research 154: 133-144. https://doi.org/10.1016/j.fcr.2013.08.005.

Chen J.M. 1996. Evaluation of vegetation indices and a modified simple ratio for boreal applications. Canadian Journal of Remote Sensing 22(3): 229-242. https://doi.org/10.1080/07038992.1996.10855178.

Cohen J. 1960. A Coefficient of Agreement for Nominal Scales. Educational and psychological measurement 20(1): 37-46. https://doi.org/10.1177/001316446002000104.

DeWald L.E., Elliott M., Sniezko R.A., and Chastagner G.A., 2018 Geographic and local variation in Pacific madrone (Arbutus menziesii) leaf blight. *In* Poster session presented at the 6th International Workshop on the Genetics of Tree-Parasite Interactions: Tree Resistance to Insects and Diseases: Putting Promise into Practice. Mt. Sterling, OH 2018.

Di Nisio A., Adamo F., Acciani G., and Attivissimo F. 2020. Fast detection of olive trees affected by *Xylella fastidiosa* from UAVs using multispectral imaging. Sensors (Basel, Switzerland) 20(17): 4915. https://doi.org/10.3390/s20174915.

DJI 2019. Matrice 200 Series - DJI. Available from https://www.dji.com/matrice-200-series.

DJI 2020. DJI Pilot - DJI Download Center - DJI. Available from https://www.dji.com/downloads/djiapp/dji-pilot.

Elliott M. 1999. Diseases of Pacific Madrone. *In* Adams A.B. (ed.). The Decline of Pacific Madrone (*Arbutus menziesii* Pursh): Current Theory and Research Directions. Seattle, Washington 1999. pp. 48-60.

Elliott M., Edmonds R., and Mayer S. 2002. Role of fungal diseases in decline of Pacific madrone. Northwest Science 76: 293-303.

Elliott M., Chastagner G.A., Dermott G., Kanaskie A., Sniezko R.A., and Hamlin J. 2012. Range-wide genetic variability in Pacific madrone (*Arbutus menziesii*): examining disease resistance, growth, and survival in a common garden study. *In* Sniezko R.A., Yanchuk A.D., Kliejunas J.T., Palmieri K.M., Alexander J.M., Frankel S.J. (tech. coords). Proceedings of the fourth international workshop on the genetics of host-parasite interactions in forestry: Disease and insect resistance in forest trees. Gen. Tech. Rep. PSW-GTR-240. Albany, CA: Pacific Southwest Research Station, Forest Service, U.S. Department of Agriculture 2012. pp. 295 - 300.

Esri 2021. ArcGIS Pro. Esri Inc., Redlands, CA.

Friedman J.H. 2001. Greedy function approximation: A gradient boosting machine. Annals of Statistics 29: 1189-1232.

Garza B.N., Ancona V., Enciso J., Perotto-Baldivieso H.L., Kunta M., and Simpson C. 2020. Quantifying citrus tree health using true color UAV images. Remote Sensing (Basel, Switzerland) 12(1): 170. https://doi.org/10.3390/rs12010170.

Geurts P., Ernst D., and Wehenkel L. 2006. Extremely randomized trees. Machine Learning 63(1): 3-42. https://doi.org/10.1007/s10994-006-6226-1.

Gitelson A.A., Kaufman Y.J., and Merzlyak M.N. 1996. Use of a green channel in remote sensing of global vegetation from EOS-MODIS. Remote Sensing of Environment 58(3): 289-298. https://doi.org/10.1016/s0034-4257(96)00072-7.

Gitelson A.A., Viña A., Ciganda V., Rundquist D.C., and Arkebauer T.J. 2005. Remote estimation of canopy chlorophyll content in crops. Geophysical Research Letters 32(8): L08403-n/a. https://doi.org/10.1029/2005GL022688.

Greenwell B.M. 2017. pdp: An R Package for Constructing Partial Dependence Plots. The R Journal 9(1): 421-436. Available from https://journal.r-project.org/archive/2017/RJ-2017-016/index.html

Group P.C. 2022. Available from https://prism.oregonstate.edu [accessed 6 Nov 2022].

Guimarães N., Pádua L., Marques P., Silva N., Peres E., and Sousa J.J. 2020. Forestry remote sensing from unmanned aerial vehicles: A review focusing on the data, processing and potentialities. Remote Sensing (Basel, Switzerland) 12(6): 1046. https://doi.org/10.3390/rs12061046.

Hijmans R.J. 2021. raster: Geographic Data Analysis and Modeling.

Hostens D.S., Dogwiler T., Hess J.W., Pavlowsky R.T., Bendix J., and Martin D.T. 2022. Assessing the Role of sUASSmall unoccupied aerial systems (sUAS) Mission DesignMission designs in the Accuracy of Digital Surface Models Derived from Structure-from-Motion Photogrammetry Photogrammetry. *In* Konsoer

K., Leitner M., and Lewis Q. (eds.) sUAS Applications in Geography. Springer International Publishing, Cham. pp. 123-156.

Hunt E.R., Daughtry C.S.T., Eitel J.U.H., and Long D.S. 2011. Remote sensing leaf chlorophyll content using a visible band index. Agronomy Journal 103(4): 1090-1099. https://doi.org/10.2134/agronj2010.0395.

Hunt E.R., Doraiswamy P.C., McMurtrey J.E., Daughtry C.S.T., Perry E.M., and Akhmedov B. 2013. A visible band index for remote sensing leaf chlorophyll content at the canopy scale. ITC Journal 21: 103-112. https://doi.org/10.1016/j.jag.2012.07.020.

Kalensky Z. and Wilson D.A. Spectral signatures of forest trees. *In* Third Canadian Symposium on Remote Sensing. 1975. pp. 155 -171.

Kuhn M. 2019. caret: Classification and Regression Training.

Landis J.R. and Koch G.G. 1977. The Measurement of observer agreement for categorical data. Biometrics 33(1): 159-174. https://doi.org/10.2307/2529310.

Lillesand T.M., Kiefer R.W., and Chipman J.W. 2015. Remote sensing and image interpretation. Seventh edition. John Wiley & Sons, Inc., Hoboken, N.J.

Lucas J.A. and Dickinson C.H. 1998. Plant pathology and plant pathogens. 3rd ed. Blackwell Science, Malden, Mass.

Maloney P.E., Lynch S.C., Kane S.F., and Rizzo D.M. 2004. Disease progression of *Phytophthora ramorum* and *Botryosphaeria dothidea* on Pacific madrone. Plant Disease 88(8): 852-857. https://doi.org/10.1094/PDIS.2004.88.8.852.

Marin D.B., de Carvalho Alves M., Pozza E.A., Belan L.L., and de Oliveira Freitas M.L. 2018. Multispectral radiometric monitoring of bacterial blight of coffee. Precision Agriculture 20(5): 959-982. https://doi.org/10.1007/s11119-018-09623-9.

Marques P., Pádua L., Adão T., Hruška J., Peres E., Sousa A., and Sousa J.J. 2019. UAV-based automatic detection and monitoring of chestnut trees. Remote Sensing 11(7): 855. Available from https://www.mdpi.com/2072-4292/11/7/855

Micasense 2019, July 25. MicaSense Altum processing workflow (including Reflectance Calibration) in Agisoft Metashape Professional 1.5. Available from https://agisoft.freshdesk.com/support/solutions/articles/31000148381-micasense-altum-processing-workflow-including-reflectance-calibration-in-agisoft-metashape-professi.

Micasense 2020. Altum - Micasense. Available from https://micasense.com/altum/.

Nesbit P.R. and Hugenholtz C.H. 2019. Enhancing UAV–SfM 3D model accuracy in high-relief landscapes by incorporating oblique images. Remote Sensing 11(3): 239. Available from https://www.mdpi.com/2072-4292/11/3/239

Oerke E.C., Gerhards R., Menz G., and Sikora R.A. 2010. Precision crop protection - the challenge and use of heterogeneity. Springer, Dordrecht.

R Core Team. 2021. R: A Language and Environment for Statistical Computing. Vienna, Austria.

Reeves S.L. 2007. *Arbutus menziesii*. Available from https://www.fs.fed.us/database/feis/plants/tree/arbmen/all.html [accessed January 11 2022].

Rouse J.W. Jr., Haas R.H., Schell J.A., and Deering D.W. 1974. Monitoring Vegetation Systems in the Great Plains with Erts. p. 309.

Sampson A.W. and Jesperson B.S. 1963. California range brushlands and browse plants. Berkeley: Division of Agricultural Sciences, University of California, Berkeley. pp. 127.

Sandino J., Pegg G., Gonzalez F., and Smith G. 2018. Aerial mapping of forests affected by pathogens using UAVs, hyperspectral sensors, and artificial intelligence. Sensors 18(4). https://doi.org/10.3390/s18040944.

Sikdar P., Mazzola M., and Xiao C.L. 2019. Genetic and pathogenic characterization of *Phacidiopycnis washingtonensis* from apple and Pacific madrone from the Western United States. Phytopathology 109(3): 469-479. https://doi.org/10.1094/PHYTO-10-17-0358-R.

Strobl C., Boulesteix A.-L., Zeileis A., and Hothorn T. 2007. Bias in random forest variable importance measures: illustrations, sources and a solution. BMC Bioinformatics 8(1): 25-25. https://doi.org/10.1186/1471-2105-8-25.

Strzepek K., Yohe G., Neumann J., and Boehlert B. 2010. Characterizing changes in drought risk for the United States from climate change. Environmental Research Letters 5(4): 044012. https://doi.org/10.1088/1748-9326/5/4/044012.

Ting K.M. 2017. Confusion Matrix. *In* Sammut C. and Webb G.I. (eds) Encyclopedia of Machine Learning and Data Mining. Springer US, Boston, MA. pp. 260-260.

Tucker C.J. 1979. Red and photographic infrared linear combinations for monitoring vegetation. Remote Sensing of Environment 8(2): 127-150. doi:10.1016/0034-4257(79)90013-0.

USDA 2006. Pacific madrone - Plant Guide. The PLANTS Database (http://plants.usda.gov). National Plant Data Team, Greensboro, NC 27401-4901 USA.

Wing M.G. 2019. Unmanned aircraft systems for remote sensing of vegetation vigor. JOJ Hortic Arboric 2(4).

Wing M.G., Burnett J., Sessions J., Brungardt J., Cordell V., Dobler D., and Wilson D. 2013. Eyes in the sky: Remote sensing technology development using small Unmanned Aircraft Systems. Journal of Forestry 111(5): 341-347. https://doi.org/10.5849/jof.12-117.

Wingtra 2022. WingtraOne GEN II Technical Specifications. Available from https://wingtra.com/mapping-drone-wingtraone/technical-specifications/ [accessed 7 Nov 2022].

Wright M.N. and Ziegler A. 2017. ranger: A Fast Implementation of Random Forests for High Dimensional Data in C++ and R. Journal of Statistical Software 77(1): 1-17. https://doi.org/10.18637/jss.v077.i01.

Zarco-Tejada P.J., González-Dugo V., and Berni J.A.J.

2012. Fluorescence, temperature and narrow-band indices acquired from a UAV platform for water stress detection using a micro-hyperspectral imager and a thermal camera. Remote sensing of environment 117: 322-337. https://doi.org/10.1016/j.rse.2011.10.007.

Zhang G.-Y., Zhang C.-X., and Zhang J.-S. 2010. Out-of-Bag Estimation of the Optimal Hyperparameter in SubBag Ensemble Method. Communications in statistics. Simulation and computation 39(10): 1877-1892. https://doi.org/10.1080/03610918.2010.521277.